



Instrument Science Report STIS 2015-03

# STIS CCD CTI Column and Temperature Dependence

---

John Biretta, Sean Lockwood, and John Debes

September 26, 2015

---

## ABSTRACT

*We derive column dependent CTI corrections for the STIS CCD detector which potentially could be used with a pixel-based CTI correction algorithm planned for the near future. Thirty-five sets of corrections are derived using the over-scan rows of internal 50CCD flats spanning 2009 to 2014. The corrections from month-to-month and year-to-year are generally well correlated and similar for most detector columns. Averaging the corrections across all datasets gives an RMS correction of 14%. Only eight columns have corrections exceeding 40%, and the range in corrections is 0.56 to 1.66. The corrections we derive are virtually identical to the preliminary corrections independently derived by Lockwood in early 2014, which did not give significant improvement in the pixel-based CTI correction. Based on this result, and similar experience for other HST instruments, we plan to omit the column corrections from the initial pixel-based CTI correction.*

*During the course of this work we discovered a strong correlation between CTI and detector housing temperature. The trailed charge due to CTI appears to increase  $\sim 2.6\%$  for each  $1^\circ\text{C}$  increase in CCD housing temperature (i.e. OCCDHTAV telemetry value). For a typical temperature range, this represents a  $\sim 16\%$  variation in CTI. We plan to incorporate this temperature dependence in future versions of the STIS pixel-based CTI corrections.*

---

## 1. Introduction

HST's current projected lifetime extends beyond 2020. For the STIS/CCD the main determinant of future performance is evolution of the detector's read noise, dark rate, sensitivity, and charge transfer inefficiency (CTI; Goudfrooij, et al., 2009, Dixon 2011) Various strategies have been considered and implemented to reduce CTI effects. The COS/STIS team, in concert with Goddard, investigated detector-level strategies to mitigate CTI, such as changing the readout time or changing the readout pattern to include two amplifiers. However, in all cases risks to the CCD's performance were seen to outweigh the potential benefits. For point source spectroscopy an effective strategy is to place the target closer to the readout amplifier, such as the "E1" pointing position, thereby reducing CTI effects. But for extended target spectroscopy and direct imaging, this approach is not always feasible. Consequently, the COS/STIS team is implementing pixel-based CTI corrections based on similar work for the ACS camera (Anderson & Bedin 2010, Lockwood, et al. 2013, 2014a ). The ACS correction model (Ogaz, et al., 2013) incorporates corrections for column-to-column CTI variation which we investigate herein for the STIS CCD. During the course of this work we also discovered a significant correlation between CTI and detector temperature variations, which should be incorporated in future versions of the pixel-based corrections.

Empirical CTI corrections are already available for target fluxes observed with the STIS CCD (Goudfrooij and Bohlin 2006, Goudfrooij, et al., 2006). These use a system of empirically derived equations to correct the target flux based on the detected counts, background counts, detector location, and epoch. The correction equations are derived from stellar observations covering a wide range of these properties. However, our new approach of pixel-based corrections has several potential advantages over the empirical corrections. Pixel-based corrections work by correcting the entire image, and hence can remove trails on cosmic ray hits and hot pixels, thereby reducing artifacts and the background noise in images. Pixel-based corrections can also provide flux correction for complex scenes which are beyond the scope of empirical flux corrections derived from stellar images. And they can also correct astrometry, and recover the true shape of resolved sources.

Column-to-column variations in CTI result from the fact that charge trapping sites are randomly distributed across the CCD detector; hence some columns of the CCD may exhibit slightly higher CTI effects than others. Ogaz, et al., 2013 have derived corrections for these column-dependent CTI variations for the ACS WFC CCD. For the case of ACS the column corrections were found to be a small effect and did not give a significant improvement in the overall CTI correction. Herein we follow the formalism developed for ACS, and derive

similar corrections for the STIS CCD detector. We use the over-scan rows which are read out after a flat-field image as a probe of CTI effects. CTI causes charge from the well-exposed flat-field image to trail into the over-scan rows. The column-to-column variations in this trailed charge provide a probe of the column variations in the CTI.

The column corrections as currently implemented are expected to provide only a statistical correction for the CTI effects in any given column. For example, it is possible that a column with excess CTI might have extra traps at some localized position within the column. Targets nearer to the read out amplifier than the excess traps would not experience them, and would hence exhibit normal CTI levels, but would receive an extra un-needed CTI correction. Targets farther from the amplifier than the excess traps would indeed experience them, and hence benefit from the column correction. So the column corrections will tend to improve the average CTI correction in some columns, though they might also corrupt data for a given target, depending on its position within the column. Ideally CTI corrections would be based on the exact locations of the traps, but this approach is beyond the current state of the art for CTI correction.

Sections 2 and 3 of this report discuss the data and analysis methods used herein to measure CTI. Section 4 describes the results on the CTI column dependence, while Section 5 discusses the discovery and measurement of CTI temperature dependence in the STIS CCD. Finally Section 6 summarizes the results.

## **2. Flat-Field Data**

Table 2 lists the flat field images used herein. All the images utilize the TUNGSTEN internal lamp, the 50CCD aperture, the MIRVIS grating, and are taken at CCDGAIN=4 with CCDAMP=D (the default amplifier). Each image contains from 5 to 12 individual exposures or frames, each of which is 0.3 seconds in duration. Typically there are 48 or 54 frames per year, though in 2009 (immediately following the repair of STIS during SM4) there are only 20 frames.

Our analysis of CTI effects will examine the CTI trail from the flat field image as it appears in the over-scan of the CCD image. The STIS CCD has a 1024 x 1024 pixel optically sensitive area. Following read-out of the optical area of the CCD detector, an additional 20 “virtual” rows are read from the detector. In an idealized detector these additional rows would contain zero counts, but in reality they will contain charge which was trapped in the CCD during readout (i.e. the CTI tail), as well as potentially other electronic signatures of the detector or readout electronics.

Besides these additional rows, additional columns are also read from the detector. Prior to, and after, the read of each CCD row, 19 virtual reads are also performed. These virtual

pixels contain information about electronic properties of the detector, and will be used during our analyses.

The virtual rows and columns appear in the `oxxxxxxxx_raw.fits` or “raw” format archive images, but not the other calibrated forms of the image. Hence the raw image is 1062 x 1044 pixels. It is useful to define a primed set of coordinates to denote pixel positions within the raw frame. If pixel positions in the raw frame are denoted by  $(x', y')$ , and the optically active area of the detector is denoted by  $(x, y)$ , the coordinates are related by equations  $x = x' - 19$  and  $y = y' - 20$ . The optical image is contained in the region by  $x' = 19$  to 1043 and  $y' = 21$  to 1044 of the raw image, or in region [20:1043,21:1044] in IRAF notation.<sup>1</sup> The “serial” or x over-scans are contained within the columns  $x' \leq 19$  and  $x' \geq 1044$ , or [1:19,1:1044] and [1044:1062,1:1044]. The “parallel” or y over-scan is contained within the rows  $y' \leq 20$  or [1:1062,1:20].

A typical 1062 x 1044 flat image, including the over-scans, is shown in Figure 1 and Figure 2. This is image `ocpj01010` from November 2014 which contains 12 independent integrations or frames. We have determined a bias level by averaging the pixels in regions [5:19,1:20] and [1044:1058,1:20] in the raw file for each individual frame, and subtracted this value from the frame. The 12 frames contained in this image were then averaged together with rejection of cosmic rays (i.e. iterative rejection of pixels more than 3 sigma above the mean), giving the image we display here.

Unlike the flats used to study the ACS column dependence, which were uniformly illuminated to the edges of the CCD, the STIS flats are highly non-uniform. The optically illuminated region of the flat varies from ~13000 counts/pixel near the center, to ~6000 counts/pixel near the upper corners of the 50CCD. More importantly, the 50CCD aperture itself blocks all direct illumination of the CCD edges. As shown in Figure 2b, the physical CCD edges still receive significant illumination due to diffractive light scattering from the 50CCD aperture edges, scattering from probable contamination on optical surfaces, and CTI tails associated with the fully illuminated portion of the image. The counts along the lowest physical row of the CCD ( $y = 1$  or  $y' = 21$ ) range from ~850 counts/pixel near the center of the row ( $x \sim 500$ ) to ~260 counts/pixel in the corners. Figure 2c shows the CTI trails in the virtual pixels or over-scan region (rows  $y' = 1$  to 20). Figure 3 plots intensity levels along a vertical slice near the center of rows  $y' = 1$  to 150, and illustrates the quantitative brightness levels associated with the illuminated flat, scattered light in the shadow of the 50CCD aperture, and the CTI tail extending into the over-scan region.

---

<sup>1</sup>We use IRAF notation where the first row (or column) at the detector edge is called “row 1” as opposed to the IDL or Python where it would be called “row 0”.

While the illumination is highly non-uniform, the data are still useful for studying column-dependent CTI effects. The CTI tail present in the over-scan will not be that immediately associated with the  $\sim 13000$  counts/pixel illumination of the flat. But rather will be associated with the scattered light in row  $y'=21$  ( $y=1$ ), together with a probable extended tail from the  $\sim 13000$  count/pixel fully illuminated flat  $\sim 15$  to  $\sim 20$  pixels away. Figure 4 shows the counts/pixel in the last physical row of the CCD ( $y'=21$ ). It is these pixels which will be primarily responsible for the counts we will later measure in the CTI tail for the first over-scan row  $y'=20$ .

**Table 1. Flats used for CTI column dependence analysis.**

Year	Image Name	Proposal ID	DATE-OBS	# Frames
2009	obas01010	11853	2009-08-31	5
''	obas02010	''	2009-09-21	5
''	obas03010	''	2009-11-09	5
''	obas04010	''	2009-12-28	5
2010	obas05010	''	2010-02-15	5
''	obas06010	''	2010-04-05	5
''	obas07010	''	2010-05-24	5
''	obas08010	''	2010-07-12	5
''	obas09010	''	2010-08-30	5
''	obas10010	''	2010-10-18	5
''	obn401010	12406	2010-12-02	6
2011	obn402010	''	2011-01-18	6
''	obn403010	''	2011-03-06	6
''	obn404010	''	2011-04-22	6
''	obn405010	''	2011-06-08	6
''	obn406010	''	2011-07-25	6
''	obn407010	''	2011-09-10	6
''	obn408010	''	2011-10-27	6
''	obut01010	12767	2011-12-02	6
2012	obut02010	''	2012-01-18	6
''	obut03010	''	2012-03-05	6
''	obut04010	''	2012-04-21	6
''	obut05010	''	2012-06-07	6
''	obut06010	''	2012-07-24	6
''	obut07010	''	2012-09-09	6
''	obut08010	''	2012-10-26	6
''	oc4x01010	13136	2012-11-05	12
2013	oc4x02010	''	2013-01-14	12

``	oc4x03010	``	2013-03-25	12
``	oc4x04010	``	2013-06-03	12
``	oceg01010	13539	2013-10-28	12
2014	oceg02010	``	2014-01-06	12
``	oceg03010	``	2014-03-17	12
``	oceg04010	``	2014-05-26	12
``	ocpj01010	13986	2014-11-03	12

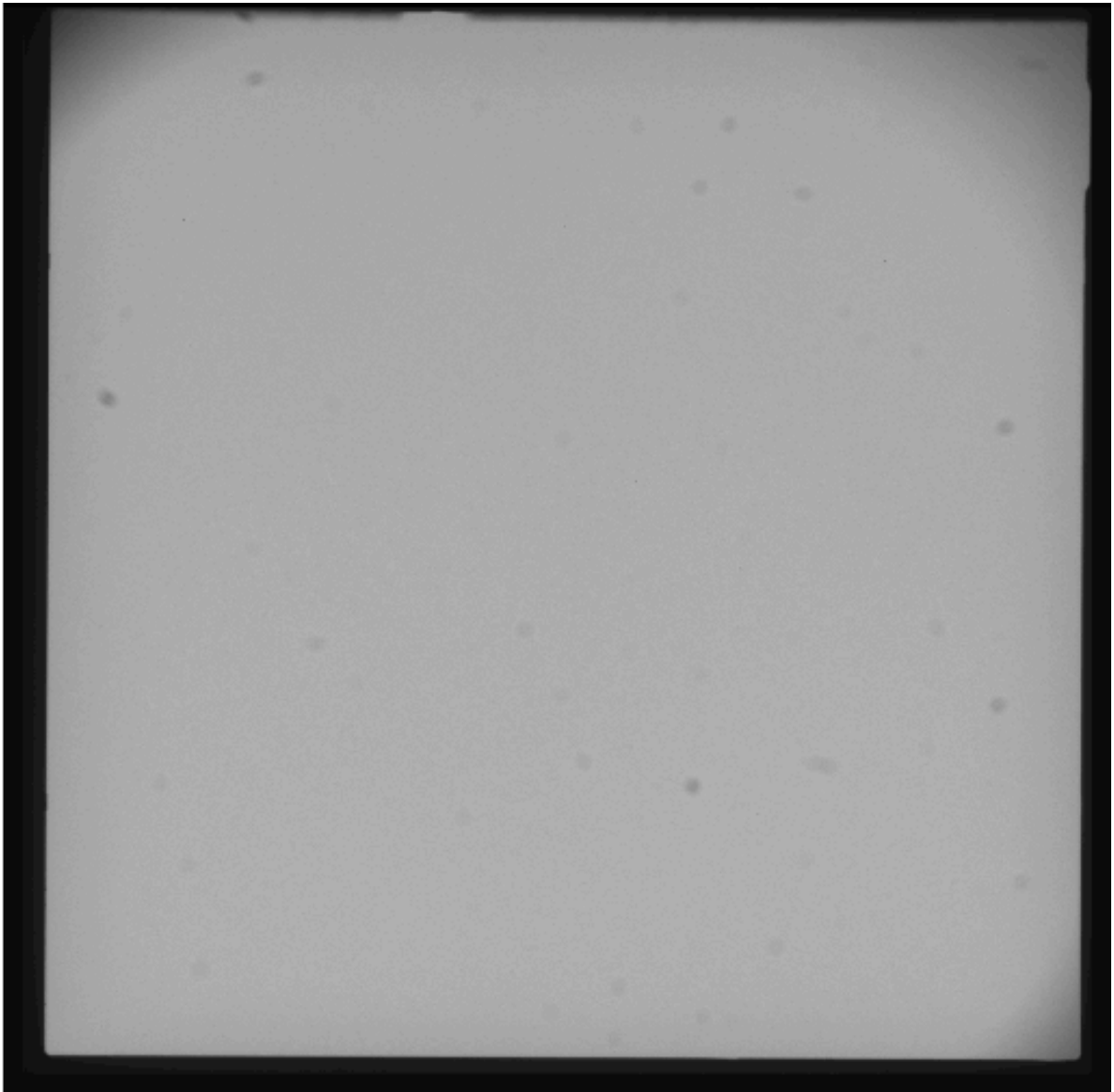


**Figure 1.** Typical “raw” format flat field image ocpj01010 from November 2014. The center of the image has  $\sim 13000$  counts/pixel, while the medium grey corners at the top left and top right are near 6000 counts/pixel. The dark border includes the region optically obscured by the 50 CCD aperture mask, as well as the virtual overscan rows and columns. The 12 frames have been bias-subtracted and averaged to remove cosmic rays (see text). The brightness scale is linear from -2000 (black) to +20000 (white) counts/pixel.

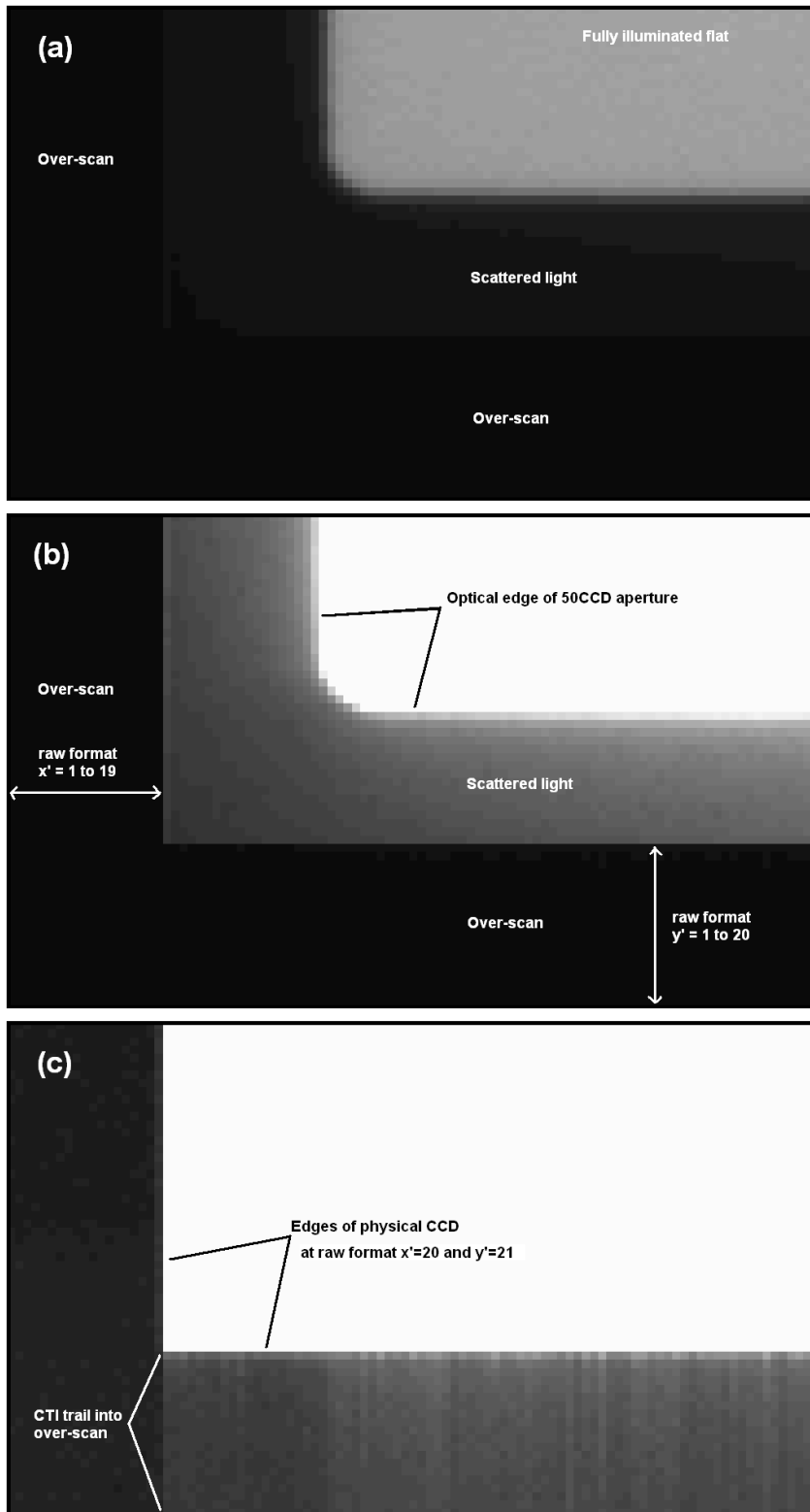


**Figure 2.** Lower left corner region [1:100,1:60] of the "raw" format image shown in Figure 1 at three different display brightness scales. Key features are labeled. The brightness scales run from (a) - 2000 (black) to 20000 (white) counts/pixel, (b) -200 to 2000, and (c) -20 to 100.

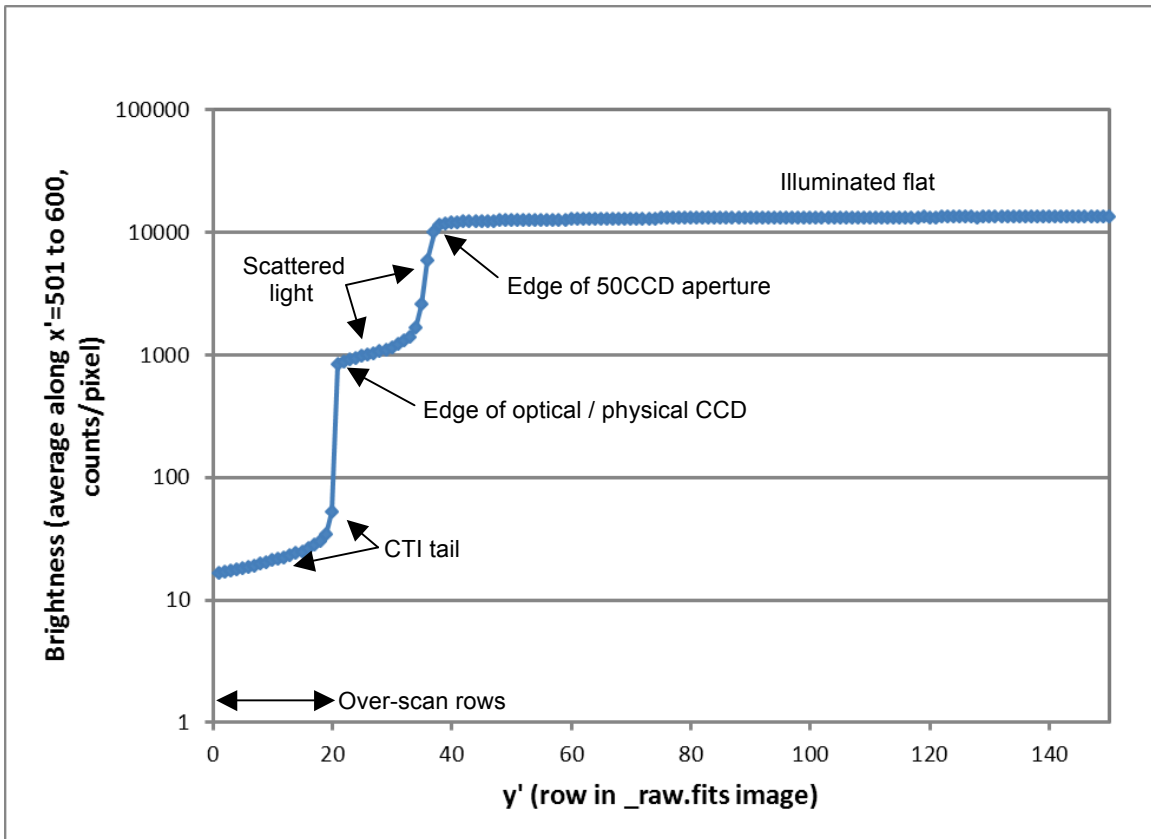
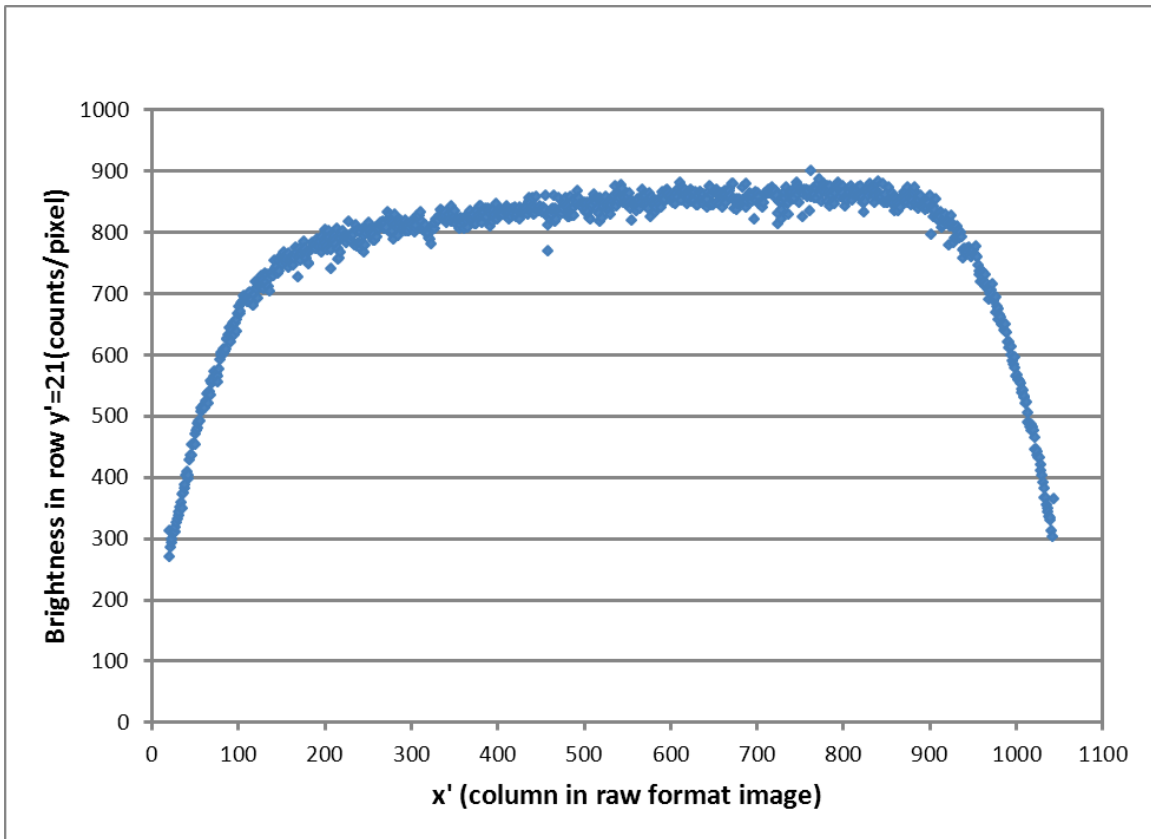


Figure 3. Average vertical slice near  $x'=550$  and extending from  $y' = 1$  to  $150$  for the same image displayed in Figure 1 and Figure 2. Columns  $x'=501$  to  $600$  have been averaged to make this plot.



**Figure 4. Brightness (counts/pixel) in last physical row of the CCD ( $x'=20$  to  $1043$ ,  $y'=21$ ) for image ocpj01010 from November 2014 (shown in Figure 1 through Figure 3). These counts represent a combination of diffraction from the 50CCD aperture edge, scattered light from any contaminants, and the CTI trail from the fully illuminated region of the flat.**

### 3. CTI Analysis

Each image listed in Table 1 was first processed in the manner already described in Section 2 to remove the bias level, and then combined and averaged with rejection of cosmic rays. The remaining procedure to compute the CTI corrections closely follows the procedure described by Ogaz, et al., 2013. First, a bias correction was made for each column: the values in rows  $y'=1$  to 10 were averaged and then subtracted from values in the first over-scan row (row  $y'=20$ ). This has the effect of subtracting any column-to-column features in the bias. It also removes much of the long CTI trail from the fully-illuminated region of the flat image ( $\sim 13000$  counts/pixel), while leaving the short CTI trail associated with the edge of the physical CCD in row  $y'=21$  whose counts are plotted in Figure 4.

The result for the November 2014 dataset ocpj01010 is shown in Figure 5. The CTI counts are typically  $\sim 34$  counts/pixels. The scatter is largely due to column-to-column variations in the CTI; the Poisson noise is estimated to be only  $\sim 1$  count/pixel. There is a gradual roll-off in the last  $\sim 150$  pixels at both ends of the row; this is largely attributable to a roll-off in the counts in the last physical row of the CCD (row  $y'=21$ , shown in Figure 4), which provides the counts that trail into over-scan row  $y'=20$ .

The final step in computing the CTI corrections is to normalize the CTI counts. We do this by computing the local average value for the CTI using a 40 pixel wide moving “boxcar” along the row, and then divide the CTI counts in each pixel by this average. This is identical to the normalization used by Ogaz, et al., 2013, except they use a slightly wider 50 pixel boxcar. At the ends of the row the boxcar width is reduce, so that the averaging does not extend outside the physical width of the CCD (i.e. the boxcar is confined to  $x'=20$  to 1043). The boxcar local average used for the normalization has been plotted in Figure 5. The resulting CTI corrections for November 2014 are shown in Figure 6. The average correction is 1.00 with an RMS of 0.14. The largest corrections are  $\sim 1.6$ . The roll-off at the row ends seen in Figure 5 has been largely removed by the normalization.

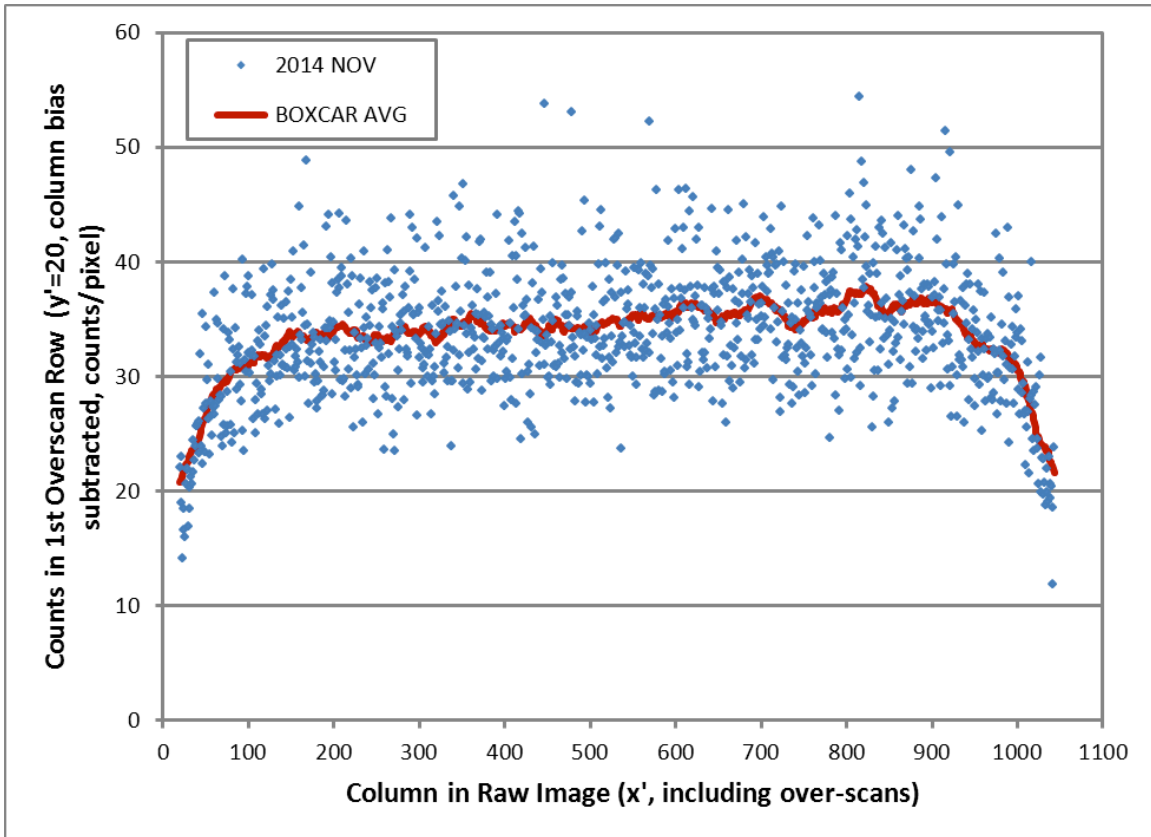
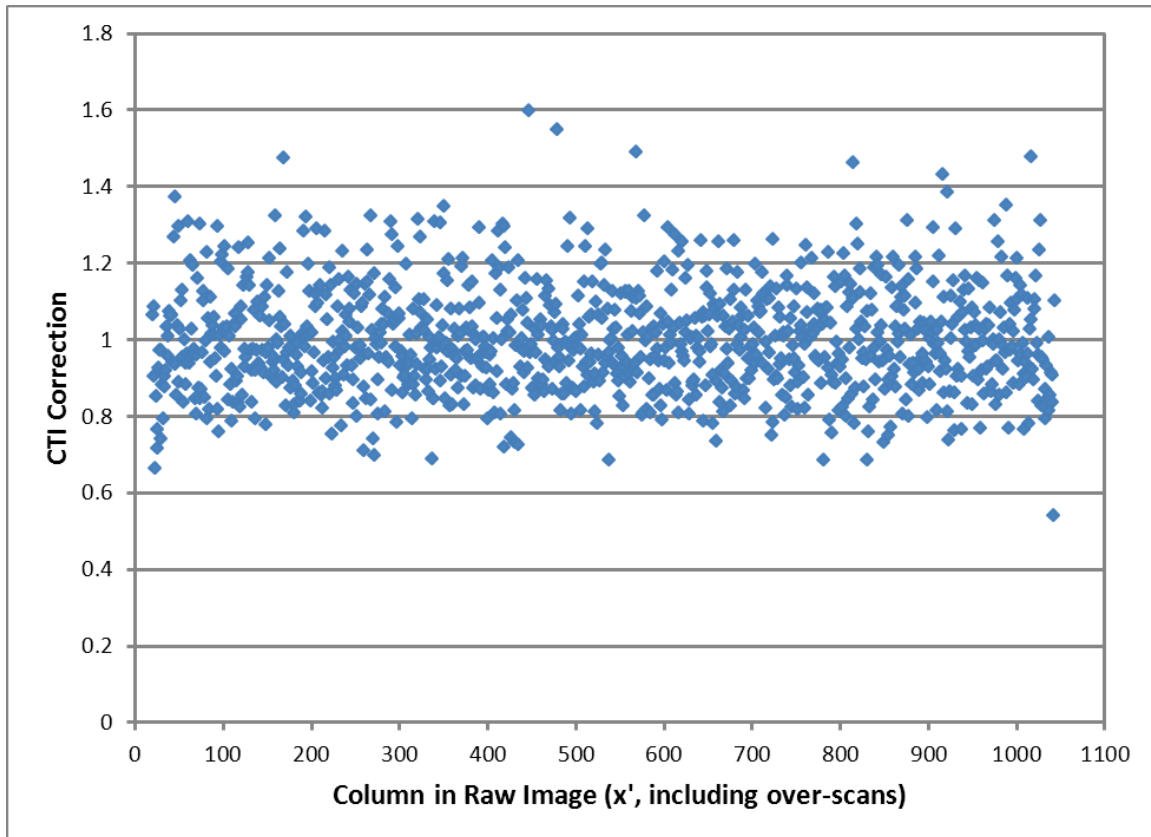


Figure 5. CTI counts/pixel in the first over-scan row  $y'=20$  for image ocpj01010 from November 2014. The average value in rows  $y'=1$  to 10 have been subtracted as a column-dependent bias correction. The local boxcar average, which will later be used to normalize the CTI corrections, is also plotted.



**Figure 6.** CTI corrections for image ocpj01010 from November 2014.

#### **4. Results: Column Dependence**

We now examine various properties of the CTI column corrections and check for probable correctness of the results. Figure 7 shows the CTI corrections at four epochs (four flats) in 2014. In general there is a good correlation of the corrections on month-to-month timescales. The scatter expected from noise is very small ( $\sim 4\%$  RMS) so the columns with larger scatter probably have some real variation in the CTI.

If we average the CTI corrections across the different flats available within each calendar year, we obtain the results shown in Figure 8. Again there tends to be a good correlation of the CTI corrections from year to year. A few columns such as  $x'=569$  show a gradual growth in the column correction from year-to-year, while most columns show a more

random variation. The uncertainty due to noise in these annual averages is  $\sim 2\%$ , except for 2009 which is  $\sim 3\%$  since it has fewer datasets.

ACS uses a single set of corrections for all epochs, which are obtained by averaging across all the available data. In Figure 9 we show similar corrections obtained by averaging across all our STIS data sets from 2009 to 2014. These average corrections may be adequate, as there tends to be good correlation of the corrections from year-to-year. The RMS of the correction is 14%, with the lowest and highest corrections being 0.56 and 1.66. Only eight columns have corrections exceeding 40%. The uncertainty due to noise in these corrections is less than 1%.

It is interesting to compare our corrections to those derived for the ACS WFC by Ogaz, et al., 2013. They state that for ACS 96% of the corrections were between 0.8 and 1.2. For STIS we find that 86% of the corrections are in this range. They do not directly quote an RMS value for the corrections, but from their Figure 6 we can estimate that the RMS scatter in the ACS corrections is about 11%. This is slightly smaller than the 14% RMS scatter we find for STIS. This larger scatter for STIS may in part be attributed to it having only 1024 pixels per column, vs. 2048 for ACS. If the trapping sites are uniformly distributed across the detector surface, the smaller number of pixels will lead to a smaller number of trapping sites per column, but a larger fractional variation in that number from column-to-column. We would expect STIS to have about  $\sqrt{2}$  larger column-to-column variations, which is approximately what is seen.

Lockwood (2014b) derived a set of preliminary CTI column corrections using all the data available at that time. These corrections are plotted against the 2009 to 2014 average corrections derived herein in Figure 10. There is excellent agreement between the two sets of corrections. While these are derived largely from the same data sets, the analyses are completely independent. Small differences are probably attributable to the extra three data sets in the present analysis. The average difference between our average 2009-2014 correction and the preliminary Lockwood correction is  $-0.1\%$  and the RMS difference is 1.7%. The largest differences (range 6% to 9%) tend to be in the first and last columns where the normalization methods differ.

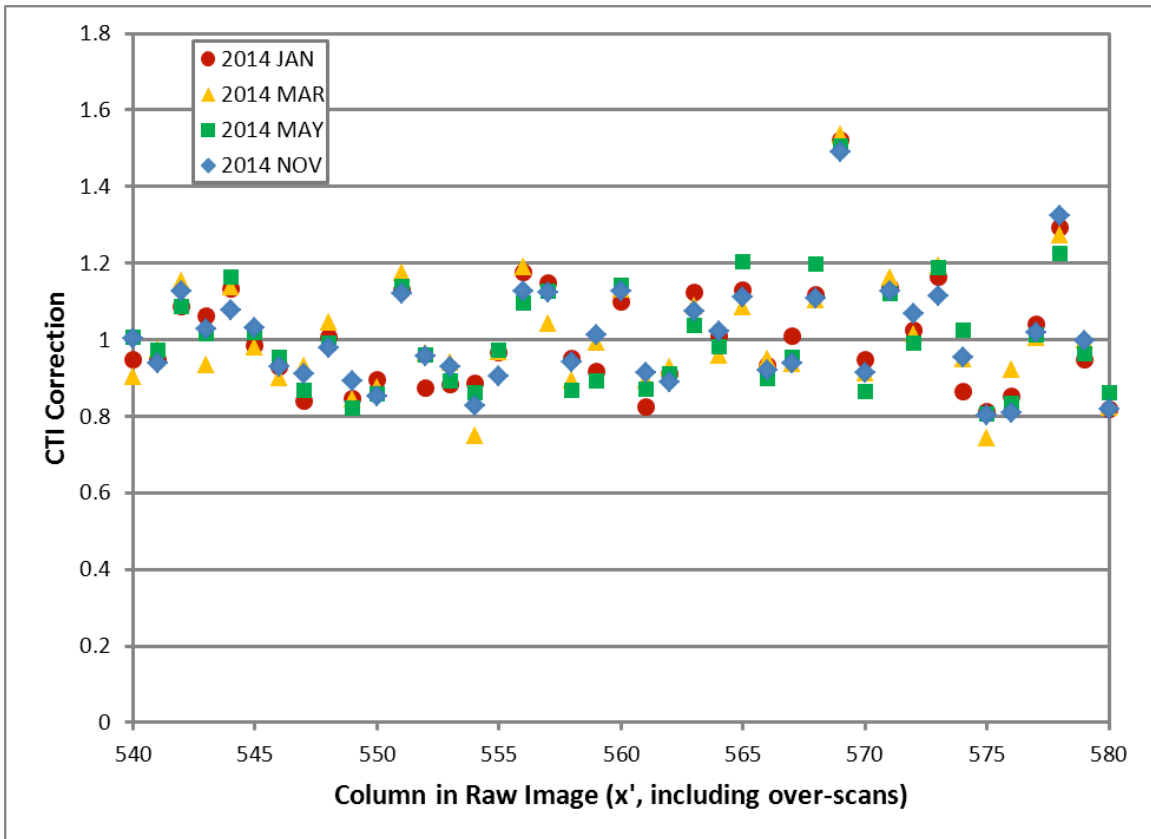


**Figure 7. CTI corrections for four epochs in 2014 over a representative range of columns from  $x'=540$  to 580.**

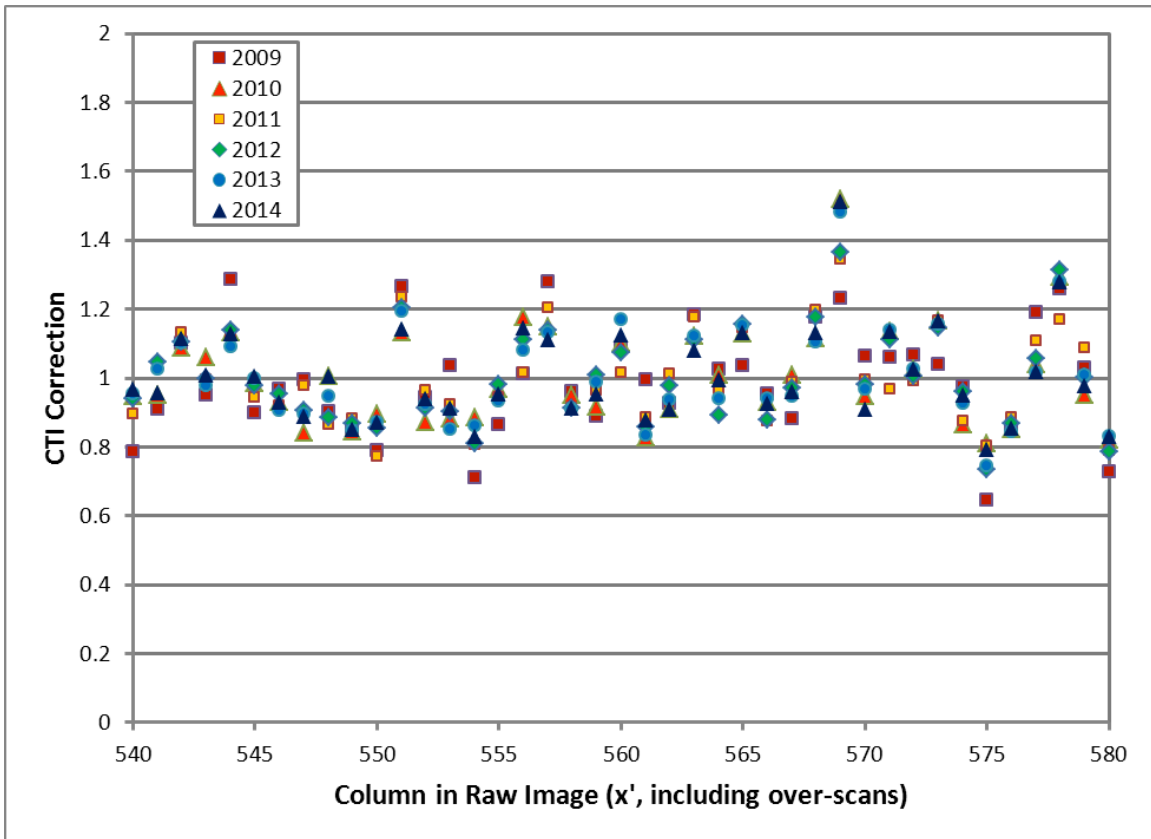


**Figure 8.** CTI corrections for each calendar year from 2009 to 2014 over a representative range of columns from  $x'=540$  to 580.

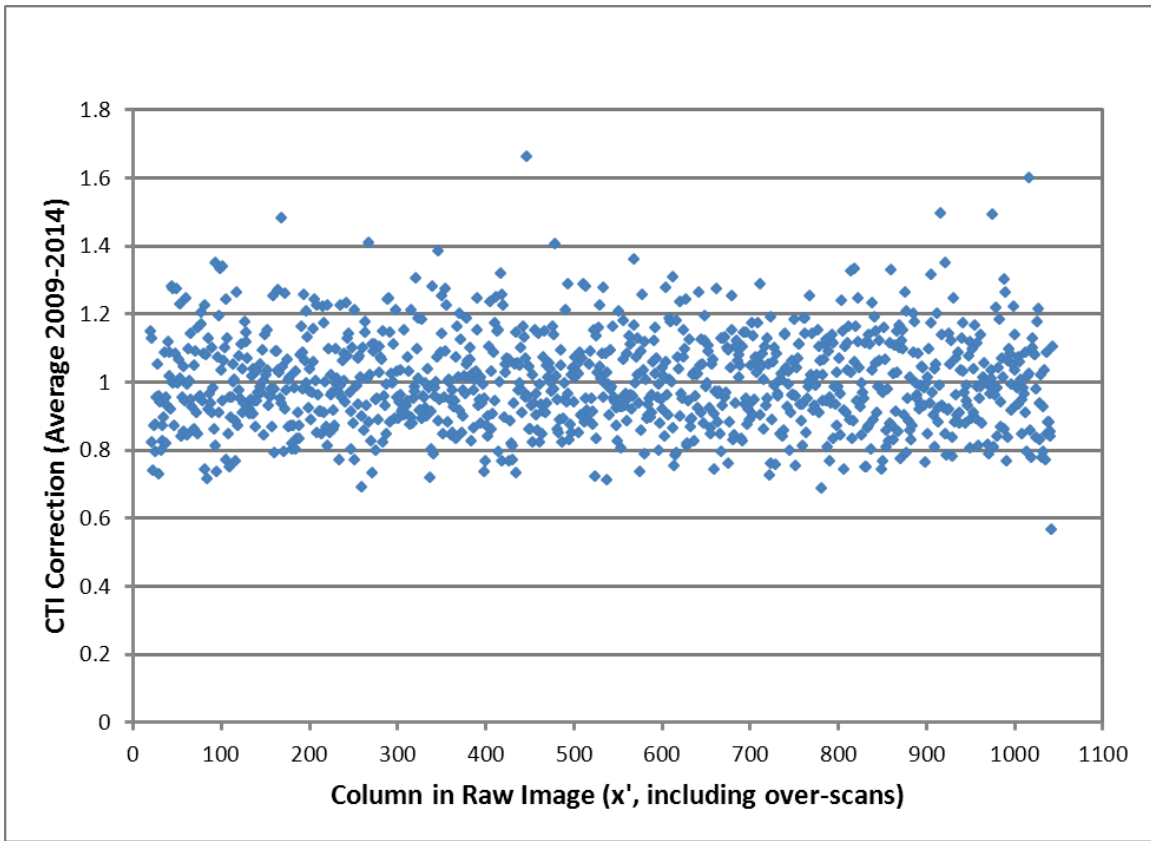


**Figure 9. Average CTI corrections for all 35 datasets spanning 2009 to 2014.**

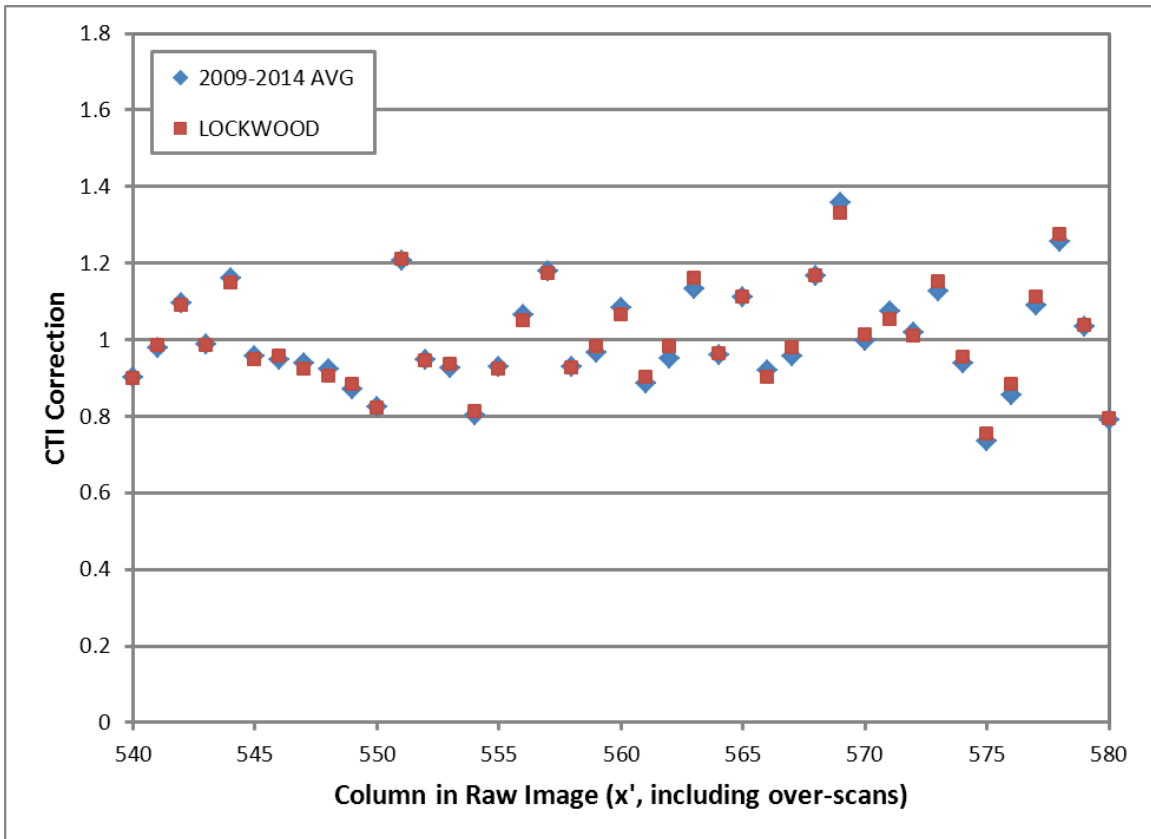


**Figure 10. Comparison of the Lockwood preliminary CTI column corrections, and the average 2009 – 2014 corrections derived herein, for a representative range of columns  $x'=540$  to 580.**

## 5. Results: Temperature Dependence

As a check on the behavior of the CTI trails and correctness of the analysis, we examined the long-term growth of the CTI. If the analyses are correct, we should see a steady linear growth of CTI with time, which extrapolates backwards to a value near zero CTI at the time STIS was placed on-orbit. This analysis led to a discovery of CTI-temperature dependence in the STIS CCD, which we now describe.

Figure 11 illustrates the average counts in the first over-scan row  $y'=20$  (averaged across columns  $x'=20$  to 1043) vs. year. Each value in Figure 11 is essentially the average of the distribution shown (e.g.) in Figure 5 for Nov. 2014 epoch; these are the values before the final step of boxcar averaging and normalization. As we see, the CTI does increase with time, as expected. There is, however, significant scatter in the points which greatly exceeds the expected noise.

We considered whether detector temperature could possibly impact the CTI. Unlike the other HST CCD detectors, the temperature of the STIS CCD has not been tightly regulated after the failure of side-1 of this instrument, and significant temperature variations are present. CTI temperature dependence has been seen in other HST instruments. Early in the Wide-Field Planetary Camera 2 (WFPC2) mission it was noted that CTI was lower at lower temperatures, and led to a decision to operate that CCD detector at the lowest available temperature set point (Trauger, et. al, 1994). A decrease in CTI was also seen in ACS WFC when the detector temperature set point was reduced in July 2006; vertical CTI decreased by about 20% when the detector temperature was reduced from  $-77\text{ }^{\circ}\text{C}$  to  $-81\text{ }^{\circ}\text{C}$  (c.f. Figure 11 in Golimowski, et al., 2011).

In Figure 12 we plot the scatter in CTI (as a ratio between the observed CTI and the linear fit vs. time) vs. the CCD housing temperature. An obvious correlation appears between the temperature and the CTI variations. The fitted line in Figure 12 corresponds to an increase in CTI by a factor of  $1.0081+0.0273*(\text{OCCDHTAV}-20)$  as the temperature increases, where OCCDHTAV is the image header value for the CCD housing temperature. Ideally the CCD detector temperature would be used here instead of the housing temperature, but we do not have access to the detector temperature on the side-2 electronics (c.f. Brown 2001). The closest value we have is the CCD housing temperature.

Once variations in CTI related to temperature were removed from Figure 11, the remaining scatter was correlated with fluctuations in the brightness of the last optical row of the CCD (row  $y'=21$ ). These fluctuations might result, e.g., from changes in the TUNGSTEN lamp brightness, or changes in contamination and scattering within the camera. Figure 13 plots this remaining scatter against the brightness averaged over the last optical row (i.e. raw image region [20:1043,21:21]). Again a significant correlation is seen, and the fitted line

corresponds to an increase in CTI by a factor of  $0.2192+0.7806*(m21/770)$ , where  $m21$  is the mean counts in the last optical row of the CCD ( $y'=21$ ). This correlation is not surprising, since it is largely these counts in row  $y'=21$  which are responsible for the CTI trail appearing in over-scan row  $y'=20$ .<sup>2</sup>

Once these correlations with temperature and brightness/scattering have been identified, it is possible to iterate the equations, and obtain an improved fit. Our final corrections used in Figure 14 are: (Observed Over-Scan Counts corrected) = (Observed Over-scan Counts) /  $[1.008935+0.025819*(OCCDHTAV-20)] / [0.2223+0.7786*(m21/770)]$ . Here the CTI increases by about 2.6% for each 1°C increase in temperature. For a typical range in CCD housing temperature of 17 °C to 23 °C, the temperature dependence represents a ~16% effect.

Figure 14 shows the long-term behavior of CTI once variations related to CCD housing temperature and brightness/scattering are removed. Ideally the fitted line would intercept zero over-scan counts (zero CTI) near the launch date of STIS in early 1997, but instead the intercept is around 1994. This may indicate some small amount of CTI present in the CCD prior to the launch of STIS, or some other long-term effect which we have not corrected. The CTI corrections described earlier in this report are self-normalized using the local boxcar averaged value, and should be immune to these long-term variations.

---

<sup>2</sup> We also attempted to correlate the over-scan counts in row  $y'=20$  with the brightness of the fully illuminated region of the flat ( $y'=50$ ), but the correlation was very poor, and we did not pursue it further.

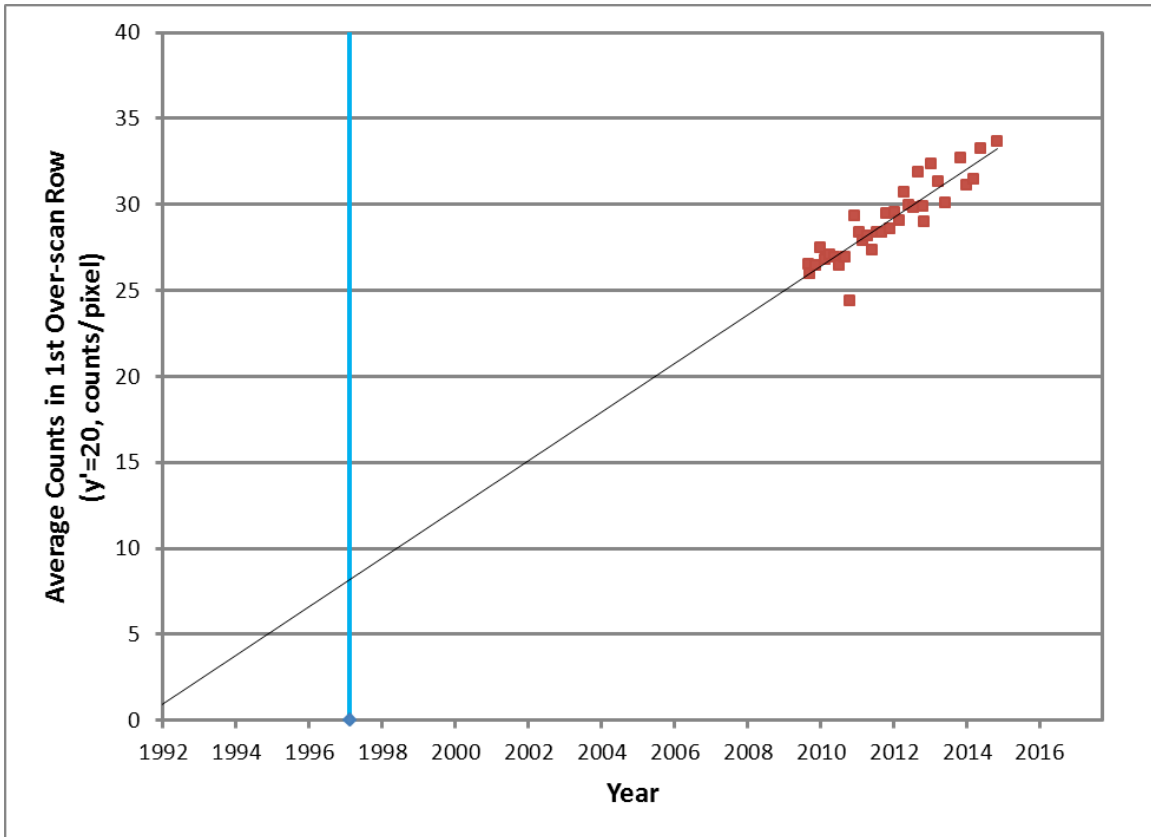


**Figure 11. Average counts in first over-scan row ( $y'=20$ ) due to CTI as function of time. The sloping line is a fit to the data points. The blue vertical line indicates the date STIS was placed on-orbit in early 1997.**

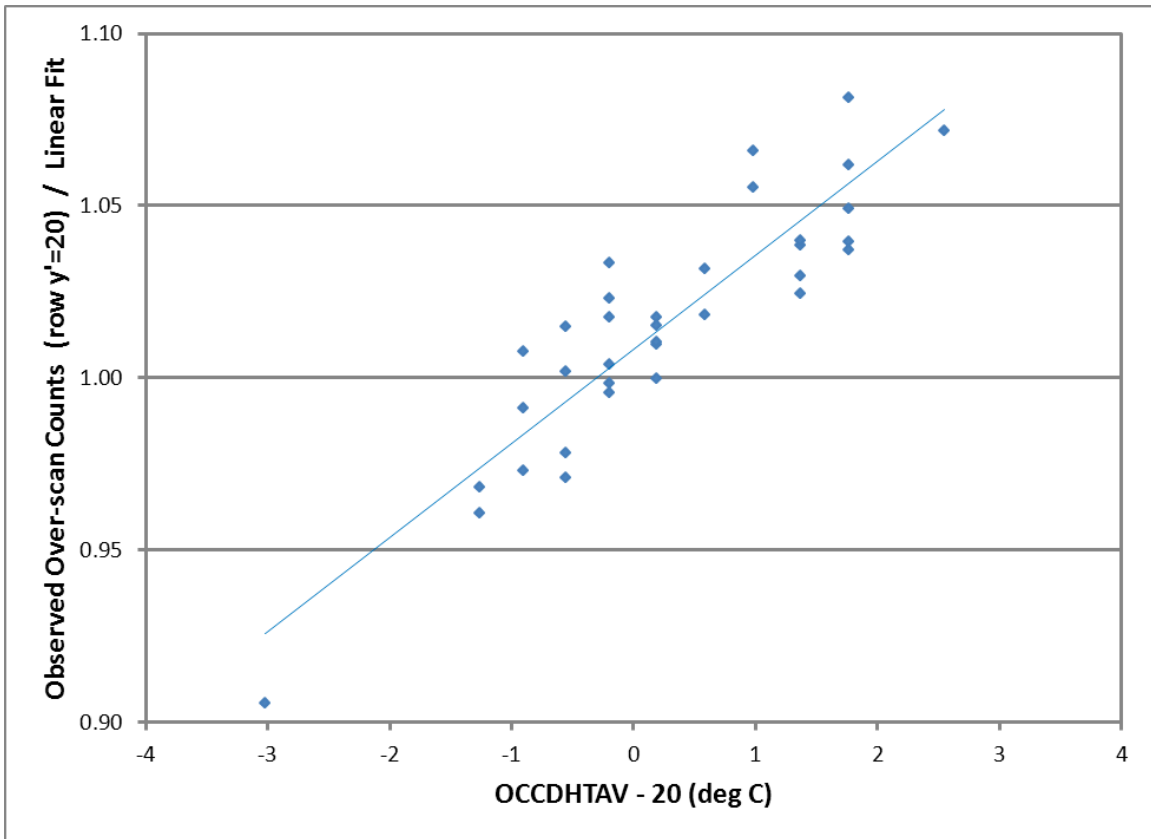


**Figure 12. Scatter around the fitted line in Figure 11 (expressed as a ratio) plotted here against the CCD housing temperature. The line fitted corresponds to  $1.0081+0.0273*(OCCDHTAV-20)$ .**

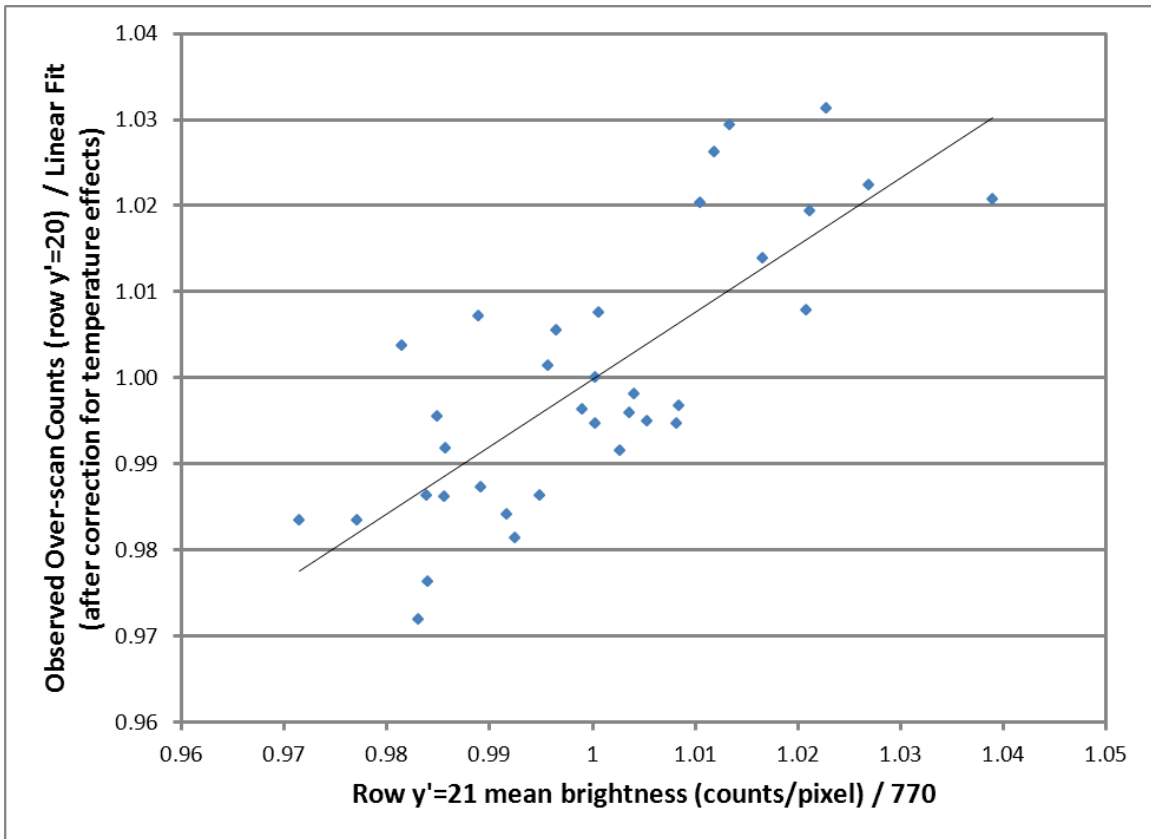


**Figure 13. Remaining scatter in Figure 11 after temperature correction (expressed as a ratio) plotted here against the mean counts in row  $y'=21$ . The line fitted corresponds to  $0.2192+0.7806*(m21/770)$ , where  $m21$  is the mean counts over region [20:1043,21:21].**

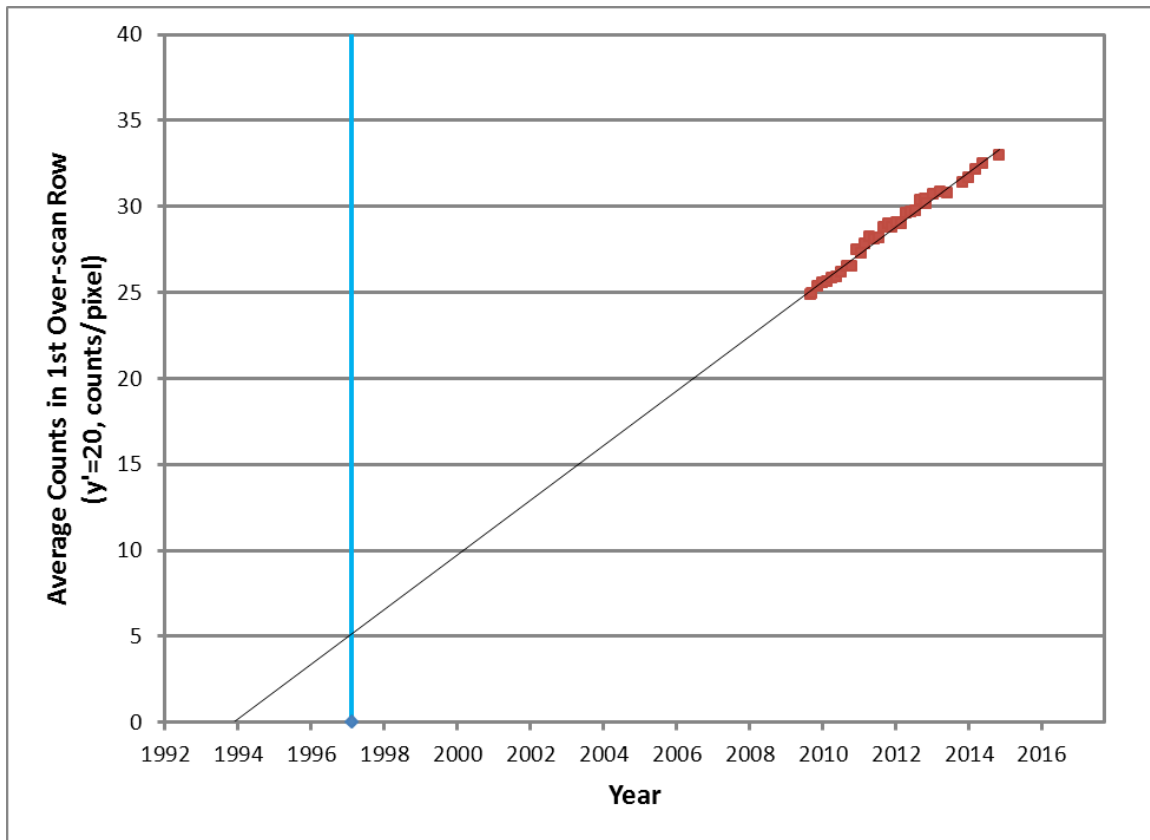


Figure 14. Same as Figure 11, but after corrections for variations in the CCD temperature and the brightness/scattering in row  $y'=21$ . The blue vertical line indicates the date STIS was placed on-orbit in early 1997.

## 6. Discussion

We have derived column dependent CTI corrections for use with the pixel-based CTI correction algorithm. Averaging across all thirty-five datasets from 2009 to 2014 gives an RMS correction of 14% between the different columns, and a range in corrections from 0.56 to 1.66. Only eight columns have corrections exceeding 40%. Our corrections are virtually identical to the preliminary ones derived by Lockwood (2014b). The STIS corrections are slightly larger than for ACS (RMS  $\sim 11\%$ ), but this may be attributed to the smaller number of pixels per column for STIS.

The preliminary CTI column corrections derived by Lockwood were tested by applying them to two different types of data. First they were tested on hot pixels in dark calibration frames.

CTI corrections were applied to the dark frames both with and without the column-dependent corrections. The column corrections did not give a significant improvement – for some hot pixels the CTI tails were reduced, while for other hot pixels they were increased (Lockwood 2014b). A second test used data from the STIS Sparse Field Calibration program. In this test a spectrum-like image is formed using a slit (rotated 90° to the usual slit orientation) together with internal lamps. The brightness and detector location of this spectrum-like image can be varied to study CTI effects (c.f. Goudfrooij, et al., 2006, Lockwood 2014c). Again pixel-based CTI corrections were applied to these data with and without the column corrections; again no clear improvement was obtained from the column corrections.

Our work here to independently derive the CTI column corrections, and finding nearly identical corrections to the preliminary work, together with a lack of improvement from the preliminary corrections, tends to indicate the column corrections are not very important for the STIS CCD. We inquired to the authors of Ogaz, et al., 2013 regarding the situation for the ACS WFC CCD, and they confirmed that the CTI column corrections gave little overall improvement for ACS (Ogaz 2015 and Anderson 2015). We also note that CTI correction work for WFC3 is proceeding without the column corrections (though they may be investigated later), again suggesting they are relatively unimportant in that instrument (Baggett 2015).

In the interest of simplicity and expediency, it is probably best to omit the column corrections from the STIS CTI corrections for now, and re-visit this topic later. A more sophisticated approach may be needed to correct the small-scale CTI variations in the detector. For example, the locations of the traps on the CCD could be mapped and then a very precise CTI correction could be made for each individual pixel.

During the course of this work we found there was excess scatter in the long-term CTI vs. time relationship, and that this scatter was strongly correlated with the temperature of the CCD detector housing. While temperature-related changes in CTI have been previously seen in WFPC2 and ACS, this is the first demonstration of this dependence in the STIS CCD. The STIS CTI appears to increase by about 2.6% for each 1 °C increase in the CCD housing temperature. For a typical temperature range of 17 °C to 23 °C, the temperature dependence results in a ~16% variation in CTI. We intend to include this temperature dependence in future pixel-based CTI corrections for STIS.

## References

- Anderson, J., and Bedin, L. R., 2010, “An Empirical Pixel-Based Correction for Imperfect CTE. I. *HST*’s Advanced Camera for Surveys,” 122, 1035.
- Anderson, J., 2015, private communication.
- Baggett, S., 2015, private communication.
- Brown, T., 2001, “Temperature Dependence of the STIS CCD Dark Rate During Side-2 Operations,” Instrument Science Report STIS 2001-03.
- Dixon, W. V. D., 2011, “Effects of CTE Degradation on Cycle 18 Observations with the STIS CCD,” Instrument Science Report STIS 2011-02.
- Golimowski, et al., 2011, “ACS after Servicing Mission 4: The WFC Optimization Campaign,” Instrument Science Report ACS 2011-04.
- Goudfrooij, P., and Bohlin, R. C., 2006, “A new CTE Correction Algorithm for Point Source Spectroscopy with the STIS CCD,” Instrument Science Report STIS 2006-03.
- Goudfrooij, P., Bohlin, R. C., Maiz-Apellaniz, J., and Kimble, R. A., 2006, “Empirical Corrections for Charge Transfer Inefficiency and Associated Centroid Shifts for STIS CCD Observations,” PASP 118, 1455.
- Goudfrooij, P., Wolfe, M. A., Bohlin, R. C., Proffitt, C. R., and Lennon, D. J., 2009, “STIS CCD Performance after SM4,” Instrument Science Report STIS 2009-02.
- Lockwood, S., et al., 2013, “Towards a Pixel-Based CTE Correction of the STIS CCD,” AAS Meeting #221.
- Lockwood, S., et al., 2014a, “Progress Towards a STIS Pixel-Based CTI-Correction,” HST Calibration Workshop, <http://www.stsci.edu/institute/conference/cal14/posters/Progress-Toward-a-STIS-Pixel-Based-CTI-Correction.pdf>
- Lockwood, S. 2014b, “Fine-Tuning CTI Correction Parameters,” [https://confluence.stsci.edu/download/attachments/50637560/cti\\_fine\\_tuning\\_v2.pdf?version=1&modificationDate=1422316072000&api=v2](https://confluence.stsci.edu/download/attachments/50637560/cti_fine_tuning_v2.pdf?version=1&modificationDate=1422316072000&api=v2) (internal project report).
- Lockwood, S. 2014c, “Measuring STIS CTI with the Internal Sparse Field Program,” <https://confluence.stsci.edu/download/attachments/50631094/Lockwood%20--%20Sparse%20Field%202014-11-25.pdf?api=v2> (internal project report).
- Ogaz, S., Anderson, J., Maybhate, A., and Smith, L., 2013, “Column Dependency in Charge Transfer Efficiency Correction,” Instrument Science Report ACS 2013-02.

Ogaz, S., 2015, private communication.

Trauger, J. T., et al., 1994, "The On-Orbit Performance of WFPC2," ApJ 435, L3.